

# Lawrence Berkeley National Laboratory

## LBL Publications

### Title

Excitation energy partition in fission

### Permalink

<https://escholarship.org/uc/item/8wc1r81p>

### Authors

Albertsson, M

Carlsson, BG

Døssing, T

et al.

### Publication Date

2020-04-01

### DOI

10.1016/j.physletb.2020.135276

Peer reviewed



## Excitation energy partition in fission

M. Albertsson<sup>a</sup>, B.G. Carlsson<sup>a</sup>, T. Døssing<sup>b</sup>, P. Möller<sup>a,1</sup>, J. Randrup<sup>c</sup>, S. Åberg<sup>a,\*</sup>

<sup>a</sup> Mathematical Physics, Lund University, S-221 00 Lund, Sweden

<sup>b</sup> Niels Bohr Institute, DK-2100 Copenhagen Ø, Denmark

<sup>c</sup> Nuclear Science Division, Lawrence Berkeley National Laboratory, Berkeley, CA 94720, USA

### ARTICLE INFO

#### Article history:

Received 26 November 2019

Received in revised form 24 January 2020

Accepted 2 February 2020

Available online 5 February 2020

Editor: J.-P. Blaizot

#### Keywords:

Fission

Brownian shape evolution method

Microscopic level densities

### ABSTRACT

The transformation of an atomic nucleus into two excited fission fragments is modeled as a strongly damped evolution of the nuclear shape. As in previous studies, it is assumed that the division of mass and charge is frozen in at a critical neck radius of  $c_0 = 2.5$  fm. In order to also determine the energetics, we follow the system further until scission occurs at a smaller neck radius, at which point the shapes of the proto-fragments are extracted. The statistical energy available at scission is then divided on the basis of the respective microscopic level densities. This approach takes account of important (and energy-dependent) finite-size effects. After the fragments have been fully accelerated and their shapes have relaxed to their equilibrium forms, they undergo sequential neutron evaporation. The dependence of the resulting mean neutron multiplicity on the fragment mass,  $\bar{\nu}(A)$ , including the dependence on the initial excitation energy of the fissioning compound nucleus, agrees reasonably well with observations, as demonstrated here for  $^{235}\text{U}(n, f)$ , and the sawtooth appearance of  $\bar{\nu}(A)$  can be understood from shell-structure effects in the level densities.

© 2020 The Author(s). Published by Elsevier B.V. This is an open access article under the CC BY license (<http://creativecommons.org/licenses/by/4.0/>). Funded by SCOAP<sup>3</sup>.

### 1. Introduction

Even 80 years after its discovery [1,2], nuclear fission remains a fertile topic for experimental and theoretical research [3–6] and improvements in instrumentation, modeling, and computation have enabled a renaissance in the field.

In their seminal paper [7], Bohr and Wheeler described fission as an evolution of the nuclear shape subject to both conservative forces from the potential energy of deformation and dissipative forces resulting from the coupling to the residual system. This conceptually simple picture suggests that the shape dynamics can be regarded as a Brownian process, as pioneered by Kramers [8].

In the limit of strong dissipation, an idealization first suggested by the recognition that the nuclear dissipation is very strong [9] the shape evolution can be simulated as a random walk by the nuclear shape [10,11] on the multi-dimensional potential-energy surface. This assumption of overdamped motion is supported by recent time-dependent density functional calculations of the whole fission process [12,13], while other calculations describe a fading

away of the dissipation in the last stages of fission, when a thin neck develops towards scission [14].

The Brownian walks are followed from well inside the fission barrier, across the barrier region, until the neck radius  $c$  has shrunk to a certain critical value,  $c_0 \approx 2.5$  fm, at which the partitioning of the nucleons between the emerging fragments is assumed to be frozen in. The resulting fragment mass distributions have been found to be in remarkably good agreement with available experimental data [10,15,16]. Furthermore, extension of the potential energy to include both neutron and proton degrees of freedom has yielded a good reproduction of the observed odd-even staggering in the fragment charge distributions [17,18].

Those simulations have generally employed potential-energy surfaces obtained by the macroscopic-microscopic method [19] and the gradual reduction of the microscopic effects as the energy is raised has been accounted for by means of an energy-dependent suppression factor containing a few adjusted global parameters [16]. A recent study [20] improved the treatment by using shape-dependent microscopic level densities to guide the Brownian evolution, thereby providing a consistent framework for calculating the energy-dependent fission-fragment yields, without the need for introducing any parameters. This refinement has made it possible to address more detailed features, such as the non-monotonic energy dependence of the symmetric fragment yield [20].

\* Corresponding author.

E-mail address: [sven.aberg@matfys.lth.se](mailto:sven.aberg@matfys.lth.se) (S. Åberg).

<sup>1</sup> Present address: P. Möller Scientific Computing and Graphics, Inc., P.O. Box 75009, Honolulu, HI 96836, USA.

We here develop the approach further by following the shape evolutions beyond the freeze-out configurations at  $c = c_0$  until effective separation of the proto-fragments occurs at a smaller neck radius,  $c = c_{sc}$ . For each such scission configuration, we extract the distorted shapes of the two nascent fragments and we then distribute the available excitation energy between those two fragments based on their microscopic level densities, calculated for their respective distorted shapes.

The degree of excitation of the fission fragments, as indicated by the corresponding mean neutron multiplicity,  $\bar{\nu}(A)$ , has long been puzzling because it appears to differ from simple statistical expectations. Most strikingly, for actinides, the light fragment typically evaporates more neutrons than the heavy fragment,  $\bar{\nu}(A_L) > \bar{\nu}(A_H)$ . However, as was recently pointed out by Schmidt and Jurado [21], previous treatments [22–24] employed the simplified Fermi-gas (Bethe) level density [25] which may be misleading at low energies where structure effects tend to be significant.

We demonstrate that a consistent use of the appropriate microscopic level densities in the distorted proto-fragments at scission provides a reasonable description of the sawtooth appearance of the fragment-mass dependence of the mean neutron multiplicity  $\bar{\nu}(A)$ .

## 2. Methodology

In our study, we generate and analyze a large number of scission configurations (typically  $10^6$ ) for the compound system  $^{236}\text{U}^*$  having a specified initial excitation energy  $E_0^*$ . For this task, we employ the Brownian shape evolution method [10], performing Metropolis walks on the potential-energy surface tabulated for the three-quadratic-surfaces (3QS) shape family [19]. These shapes [26] are characterized by five parameters: the overall elongation given by the quadrupole moment  $Q$ , the radius  $c$  of the hyperbolic neck between the two spheroidal end sections which have deformations  $\varepsilon_{f1}$  and  $\varepsilon_{f2}$ , and the mass asymmetry  $\alpha$ .

Each Metropolis walk is started in the second minimum and continued across and beyond the outer barrier through the freeze-out at  $c = c_0$  (where the mass division is frozen out) and until a scission configuration is reached at  $c = c_{sc}$ . We regard the value of this quantity as being somewhat adjustable; here we use the value  $c_{sc} = 1.5$  fm determined in Ref. [27] as leading to good agreement with the measured fragment kinetic energies. The mass numbers of the nascent heavy and light fragments,  $A_H$  and  $A_L$ , are determined by the value of the 3QS asymmetry parameter  $\alpha$  at freeze-out. The associated fragment charge numbers,  $Z_H$  and  $Z_L$ , are selected as those values that best preserve the  $N:Z$  ratio. For the present exploratory study, we consider only divisions into even-even fragments.

We assume that the scission shape is transformed into two proto-fragments that have spheroidal shapes characterized by the 3QS  $\varepsilon_2$  values at scission,  $\varepsilon_H^{sc}$ , and  $\varepsilon_L^{sc}$ . These generally differ from the corresponding ground-state deformations,  $\varepsilon_i^{gs}$  (including also  $\varepsilon_4$  and  $\varepsilon_6$  deformations). The associated distortion energies,  $E_{\text{dist},i} = M_i(\varepsilon_i^{sc}) - M_i(\varepsilon_i^{gs})$ , are converted into statistical fragment excitations later on as the fragment shapes relax to their ground-state forms. The shape-dependent fragment masses,  $M_i(\varepsilon)$ , are calculated in the same macroscopic-microscopic model that was used to obtain the potential-energy surfaces [28].

Because the collective kinetic energy associated with the shape evolution is assumed to be negligible prior to scission (see Refs. [9, 12, 13]), we take the available excitation energy at scission to be the difference between the total energy,  $E_{\text{tot}}$ , and the potential energy of the scission configuration,

$$E_{sc}^* = E_{\text{tot}} - U(Q_{sc}, c_{sc}, \varepsilon_1^{sc}, \varepsilon_2^{sc}, \alpha_{sc}). \quad (1)$$

In the present study, we assume that this quantity is divided statistically between the two fragments, *i.e.* the total excitation energy of the heavy fragment,  $E_H^*$ , is governed by the following micro-canonical distribution,

$$P(E_H^*; E_{sc}^*) \sim \tilde{\rho}_H(E_H^*; \varepsilon_H^{sc}) \tilde{\rho}_L(E_{sc}^* - E_H^*; \varepsilon_L^{sc}), \quad (2)$$

and  $E_L^* = E_{sc}^* - E_H^*$  due to energy conservation, where  $\tilde{\rho}_i(E_i^*; \varepsilon_i^{sc}) \equiv \tilde{\rho}(N_i, Z_i, E_i^*; \varepsilon_i^{sc})$  is the effective density of states (see below) of a nucleus with neutron and proton numbers  $N_i$  and  $Z_i$ , spheroidal deformation  $\varepsilon_i$ , and a total excitation energy of  $E_i^*$ , with  $i = H, L$ . Because the fragment deformations at scission generally differ from their ground-state values there is no experimental information available on the required level densities. Instead, an established microscopic model is employed to calculate the energy partition distribution function Eq. (2).

The key novelty of the present study is the use of shape-dependent microscopic level densities in the above expression (2) for the partitioning of the available energy. The fragment level densities are calculated by employing the combinatorial method of Ref. [29], to the same model as that giving the shape-dependent compound nuclear level density employed in the Metropolis walk. Thus, for each proto-fragment, the neutron and proton wave functions are calculated in the spheroidal effective field and the many-quasi-particle excitations are constructed. For each such configuration, a BCS pairing calculation is carried out and the associated rotational band is built. For each value of the angular momentum  $I$ , the level density  $\rho(E^*, I; \varepsilon^{sc})$  is then extracted by counting the number of energy levels having angular momentum  $I$  in a small energy interval around  $E^*$ . In the present study, we are interested in the energy distribution only, so we sum over the fragment angular momentum,  $I_i$ , to obtain the effective density of states entering in Eq. (2),

$$\tilde{\rho}_i(E_i^*; \varepsilon_i^{sc}) = \sum_{I_i} (2I_i + 1) \rho_i(E_i^*, I_i; \varepsilon_i^{sc}). \quad (3)$$

## 3. Results

Fig. 1 shows the energy distribution  $P(E_H^*, E_{sc}^*)$  at three different values of the total available energy  $E_{sc}^*$  for two different mass divisions having  $(A_H:A_L) = (130:106)$  and  $(152:84)$ . These two divisions contribute to the yields at the inner and outer wings of the double-humped mass distribution, respectively, (see *e.g.* Fig. 9 of Ref. [20]), and the deformations considered are typical of those divisions.

The energy distribution was calculated with both the microscopic level density discussed above and a simple macroscopic (Fermi-gas) level density,  $\rho_{FG}(E^*) \sim \exp[2\sqrt{aE^*}]$  with  $a=A/(8 \text{ MeV})$ . Both yield rather broad distributions due to the smallness of the nuclear system. The macroscopic form yields smooth Gaussian-like distributions peaked at  $E_H^*/E_L^* = A_H/A_L$ , whereas the microscopic form yields irregular distributions that may have qualitatively different appearances, especially at lower values of  $E_{sc}^*$  where quantal structure effects are most significant. In particular, it is possible that one fragment receives all the available energy with the partner fragment being left without excitation. Although the probability for this decreases quite rapidly with increasing  $E_{sc}^*$ , this feature is in dramatic contrast to the macroscopic result.

The mechanism for the energy partitioning considered here differs from the idealized “energy sorting mechanism” proposed in Ref. [21], where all energy is transferred to one fragment, namely the one with the lowest temperature. The finite size of the nuclear

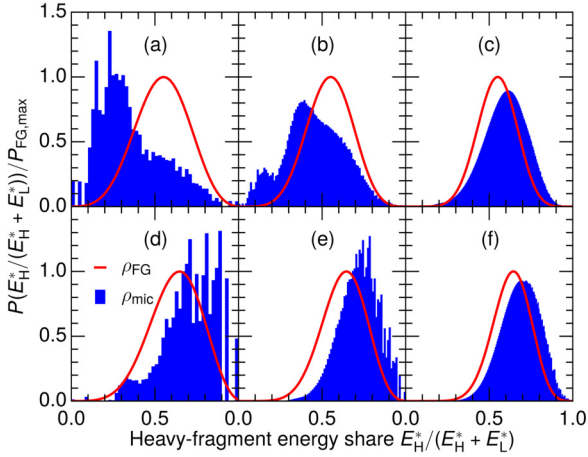


**Fig. 1.** The distribution function  $P(E_H^*; E_L^*)$  for the total excitation of the heavy fragment in  $^{235}\text{U}(n, f)$  for two different divisions, either  $(N, Z, \varepsilon)_H = (80, 50, -0.1)$  and  $(N, Z, \varepsilon)_L = (64, 42, 0.3)$  (top panels) or  $(N, Z, \varepsilon)_H = (92, 60, 0.1)$  and  $(N, Z, \varepsilon)_L = (52, 32, 0.1)$  (bottom panels), and three different values of the available energy at scission,  $E_{sc}^* = 10$  (left column), 20 (center column), 40 (right column) MeV. The distributions obtained from microscopic (blue histograms) and Fermi-gas (solid red curves) level densities are normalized to the maximum value of the Fermi-gas result.

system always leads to a broad distribution of the fragment excitations, as seen in Fig. 1, where both fragments have an appreciable chance for receiving part of the energy.

For the case shown in the top panel of Fig. 1, the heavy fragment is  $^{130}\text{Sn}$  which is very close to being doubly magic. It therefore has a spherical ground-state shape,  $\varepsilon_H^{\text{gs}} = 0$ , while the light fragment,  $^{106}\text{Mo}$ , has a well-deformed prolate ground-state shape,  $\varepsilon_L^{\text{gs}} = 0.33$ . The fragment deformations at scission are  $\varepsilon_H^{\text{sc}} = -0.10$  and  $\varepsilon_L^{\text{sc}} = 0.30$  which both deviate only slightly from the ground-state deformations. The near magicity of the heavy fragment (which has a shell correction energy of  $-10.2$  MeV) causes the level density to remain very small up to excitation energies of 20 MeV. Conversely, the shell correction energy of the light fragment is  $+0.35$  MeV and its level density is considerably larger than that of the heavy partner in that energy range. As a consequence, the energy distribution is peaked at small values of  $E_H^*$  and the major part of the energy goes to the light fragment. For example, when the total energy available for sharing is 10 MeV, the most likely outcome is that the heavy fragment receives only  $\approx 2$  MeV, while the light fragment gets  $\approx 8$  MeV. This is very different from the macroscopic (Fermi-gas) scenario in which the most likely excitations of those fragments are about 5.5 and 4.5 MeV, respectively.

A different picture appears in an example when the two fragments differ more in size, as illustrated in the bottom panel of Fig. 1. Here the microscopic energy-partition distribution function strongly favors the heavy fragment,  $^{152}\text{Nd}$ , relative to the light fragment,  $^{84}\text{Ge}$ . In this case, the typical scission deformation of the heavy fragment is considerably smaller,  $\varepsilon_H^{\text{sc}} = 0.10$ , than its ground-state deformation,  $\varepsilon_H^{\text{gs}} = 0.24$ . Therefore the heavy fragment has a large single-particle level density and, consequently, it has a large positive shell correction energy,  $+6.1$  MeV (as compared to  $-6.9$  MeV for the ground-state shape) and a particularly high level density. On the other hand, the neutron number of the light fragment,  $N_L = 52$ , is close to being magic so its level density is low. As a result, the heavy fragment is strongly favored in the energy division, even up to quite high energies, as clearly seen in Fig. 1 (d)-(f).

As the available energy is increased, the microscopic energy partition distribution (2) approaches the macroscopic form ob-

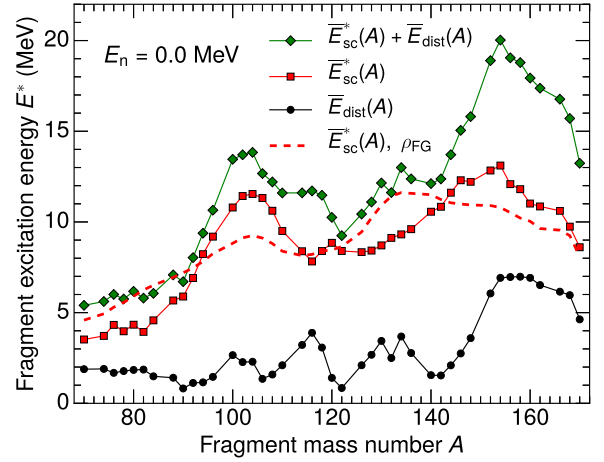


**Fig. 2.** The mean fragment distortion energy  $E_{\text{dist}}^*(A)$  (black dots), the mean excitation energy at scission,  $E_{\text{sc}}^*(A)$  (red squares), and the sum,  $E_{\text{dist}}^*(A) + E_{\text{sc}}^*(A)$  (green diamonds), as extracted from an ensemble of  $10^6$  scission configurations, are shown as functions of the fragment mass number  $A$ . For reference is also shown  $E_{\text{sc}}^*(A)$  obtained with the simple Fermi-gas level density (red dashed curve).

tained with the Fermi-gas level density [20] and the structure effects on the mass partition subside, albeit at various rates.

For each scission configuration obtained at the end of the Metropolis walk, the excitation energies of the nascent fragments are sampled from the appropriate microscopic partition distribution (2) illustrated in Fig. 1. For  $^{235}\text{U}(n_{\text{th}}, f)$ , the resulting mean excitation energy  $\bar{E}_{\text{sc}}^*(A)$  is shown in Fig. 2 as a function of the fragment mass number  $A$ , together with the mean fragment distortion energy  $\bar{E}_{\text{dist}}^*(A)$ , as well as the sum of these two quantities which represents the total excitation energy of the fragment relative to its ground state.

To illustrate the effect of the microscopic level densities, Fig. 2 also shows the mean excitation energy obtained with the simple Fermi-gas level density. The structure of the undulating difference between the two curves,  $\Delta E_{\text{sc}}^*(A) \equiv E_{\text{sc}, \text{mic}}^*(A) - E_{\text{sc}, \text{mac}}^*(A)$ , can be qualitatively understood from the two energy partition distribution functions discussed above. The local minimum in  $\Delta E_{\text{sc}}^*(A)$  slightly below  $A = 130$  and its local maximum around  $A = 106$  result from the favoring of the light fragment in the energy sharing illustrated in Fig. 1 (a) – (c), while the pronounced maximum of  $\Delta E_{\text{sc}}^*(A)$  at  $A \approx 150$  and the corresponding minimum around  $A \approx 84$  result from the favoring of the heavy fragment illustrated in Fig. 1 (d) – (f).

With regard to the distortion energies, we note that the scission shapes are typically less deformed than the corresponding ground-state shapes,  $\varepsilon_i^{\text{sc}} < \varepsilon_i^{\text{gs}}$ . The resulting mean distortion energies increase from 2–3 MeV for light fragments to 6–7 MeV for heavy fragments. As a consequence, the maximum in  $\bar{E}_{\text{sc}}^*(A)$  around  $A = 150$  is enhanced by the large distortion energies in the same mass region, as is clearly brought out in Fig. 2.

After scission, the fragments are accelerated by their Coulomb repulsion, and their shapes relax towards the ground-state shapes. We assume that the relaxation of the shapes occurs at a shorter time scale than the subsequent neutron evaporation. In this picture, neutrons are evaporated from fragments in their ground-state deformation, starting out with the full excitation energy  $E_{\text{sc}}^* + E_{\text{dist}}$ . The higher this energy, the more neutrons can be evaporated. Thus, experimental information on the average number of neutrons emitted  $\bar{\nu}(A)$  as function of the fragment mass carries information on the energy partitioning of the excitation energy of fragments. We therefore proceed to calculate neutron evaporation from the fragments.

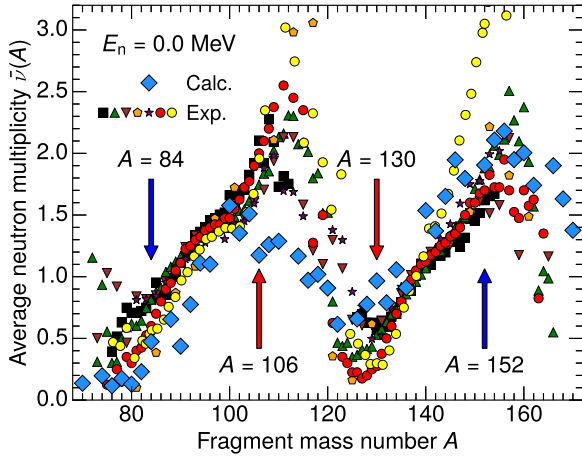


**Fig. 3.** The calculated mean neutron multiplicity  $\bar{\nu}(A)$  (blue diamonds) for  $^{235}\text{U}(n, f)$  is shown as a function of the mass number of the primary fission fragment, which is compared to a variety of experimental data: black squares [30], yellow circles [31], green triangles [32], orange diamonds [33], purple stars [34] brown triangles [35], red circles [36]. The red/blue arrows point to the mass divisions selected in Fig. 1.

Because the initial compound excitation energies are relatively low, neutron emission prior to or during fission is insignificant. Furthermore, the fragment angular momentum  $I$  is hardly affected by the evaporation, so the energy available for neutron evaporation is taken as  $E = E^* - \bar{E}_{\text{rot}}$ , where  $\bar{E}_{\text{rot}}$  is the average rotational energy (which will later contribute to the photon radiation). For a given fragment ( $Z, N, E, \varepsilon$ ), the kinetic energy  $\varepsilon_n$  of the evaporated neutron is sampled from the spectrum  $\sim \bar{\rho}'(E'; \varepsilon') \varepsilon_n$ , where  $\bar{\rho}'$  denotes the effective level density in the daughter fragment ( $Z' = Z, N' = N - 1, E' = E - \varepsilon_n - S_n, \varepsilon'$ ), with  $S_n$  being the neutron separation energy in the mother fragment. (Though not important for the present study, to be consistent we employ the microscopic level density (3) for the evaporation daughter nucleus.) Following the treatment in Ref. [40], the neutron evaporation is continued until the excitation energy has fallen below the neutron separation energy.

Fig. 3 shows the calculated mean neutron multiplicity  $\bar{\nu}(A)$  together with experimental data from a variety of experiments. (A related analysis for  $^{240}\text{Pu}$  was performed in Ref. [13].) The observed sawtooth behavior (minima at  $A \approx 76, 126$  and maxima at  $A \approx 110, 156$ ) is reasonably well reproduced by the calculation and arises from a combined effect of the behavior of the neutron separation energy  $S_n(A)$ , which displays a jump near  $A = 132$  due to the closed shells at  $Z = 50$  and  $N = 82$ , and the behavior of the total intrinsic fragment energy  $E_{\text{dist}}(A) + E_{\text{sc}}^*(A)$  (see Fig. 2). Indeed, the energy partition determined by microscopic level densities (as compared to Fermi-gas level densities) implies an enhanced neutron emission for  $A \sim 106$  and  $A \sim 150$ , and correspondingly less neutrons emitted for  $A \sim 130$  and  $A \sim 84$ .

The shortfall of  $\bar{\nu}(A)$  in the region around  $A = 110$  arises from the fact that the Brownian shape evolution leads to too large fragment kinetic energies for mass divisions near symmetry, possibly because the 3QS shape family employed is inadequate for those very elongated scission configurations. (If the kinetic energies are adjusted to correct for this shortcoming, the agreement of  $\bar{\nu}(A)$  with data is significantly improved [27].)

The energy dependence of the energy partitioning is illustrated in Fig. 4 which shows  $\bar{\nu}(A)$  resulting from first-chance fission at three different incident neutron energies. The experimental data from Ref. [41] are also shown. As the energy is raised, the structure effects in the level densities smear out and the undulations in  $\bar{\nu}(A)$  diminish. In the region around  $A = 130$ , the very low neutron

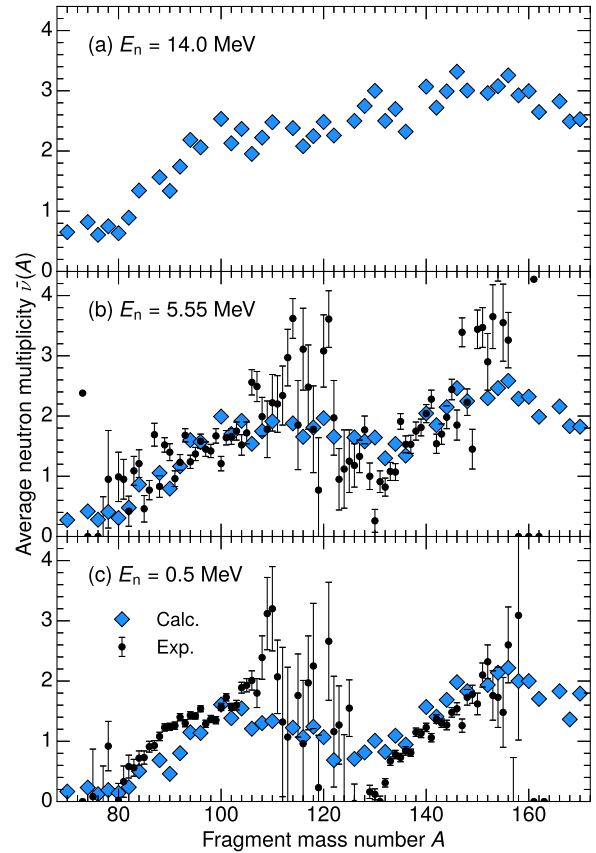


**Fig. 4.** For  $^{235}\text{U}(n, f)$  is shown the calculated mean neutron multiplicity as a function of the mass number of the primary fission fragment,  $\bar{\nu}(A)$ , for three different incident neutron energies  $E_n$ : 0.5 MeV (a), 5.55 MeV (b), 14 MeV (c). The experimental data from Ref. [41] are also shown.

multiplicity occurring for thermal fission grows rather rapidly with increasing neutron energy, causing the sawtooth feature of  $\bar{\nu}(A)$  to weaken. This behavior is due to the decrease of the strong negative shell correction at higher excitation energy for fragments in this mass region, increasing the level density and thus the share of the excitation energy taken up by the heavy fragment at scission. On the contrary, the neutron multiplicity from the light fragments is affected much less by the increase in energy. Indeed, as  $E_n$  is increased from 0.5 to 5.55 MeV the measured [41] mean neutron multiplicity grows by 0.04 and 0.69 for light and heavy fragments, respectively, while the corresponding calculated increases are 0.20 and 0.54.

#### 4. Summary and discussion

For the purpose of elucidating the importance of structure effects for the degree of excitation of the primary fission fragments, we have augmented the recently developed level-density guided Metropolis shape evolution treatment [20] with shape-dependent microscopic level densities for the nascent proto-fragments which are distorted relative to their equilibrium shapes. The available energy is partitioned microcanonically according to the corresponding microscopic level densities which take account of the structure effects for these non-equilibrium shapes. For each fragment, the distortion energy is converted into additional excitation before the neutron evaporation cascade begins. Apart from the symmetry region where the 3QS shape family appears to be inadequate and leads to too little statistical excitation, the dependence of the resulting mean neutron multiplicity on fragment mass,  $\bar{\nu}(A)$ , agrees

reasonably well with the experimental data. In particular, the sawtooth appearance of  $\bar{\nu}(A)$  can be understood from shell-structure effects in the level densities as well as from structure in the distortion energy surface.

We also studied how  $\bar{\nu}(A)$  changes as the excitation energy of the fissioning nucleus is increased. The sawtooth behavior is weakened due to the reduction of the shell corrections near  $A = 130$  which significantly increases the level density in the heavy fragment and therefore  $\bar{E}_{sc}^*(A_H)$ , hence also  $\bar{\nu}(A_H)$ . Such an evolution is also seen in the experimental data. It is thus our conclusion that the microscopic sharing mechanism studied here contributes significantly to the observed sawtooth behavior.

In our treatment, the characteristic feature that relatively few neutrons are emitted from the heavy  $^{132}\text{Sn}$ -like fragments and relatively many from the light partner fragments emerges mainly because of the shell effects in the level-densities. This mechanism differs from some previous studies where similar results were obtained with less (or no) excitation energy but with a very deformed light fragment (hence a large  $\bar{E}_{dist}(A_L)$ ) and a nearly spherical heavy fragment, leading to conversion of deformation energy for the light fragment into emitted neutrons [38,39]. In both scenarios the sawtooth appearance of  $\bar{\nu}(A)$  is related to the shell effects associated with a spherical shape of the heavy fragment.

In recent calculations [12,13,37] octupole deformations of the fission fragments are found to play an important role in the fission dynamics. In some cases, this significance is related to shell-stabilized octupole deformations of specific isotopes [37]. In our calculations the parametrized fragment shapes are limited to quadrupole deformations defined from the edge shape parameters in the 3QS shape family. It would certainly be interesting (but time consuming) to include octupole shapes of each proto-fragment as well.

The total excitation energy in the two fragments is reflected in the resulting neutron multiplicity and is thus experimentally accessible, whereas it is less obvious how to determine how much of that energy was present as statistical excitation already at scission and how much was recovered later from the proto-fragment distortions. Careful analysis of the detailed form of  $\bar{\nu}(A)$  may identify observable differences between the two mechanisms, but this may require more accurate experimental data.

Finally, we wish to note that the presented treatment stays within the well-established framework of the macroscopic-microscopic model of nuclear structure underlying the calculation of the nuclear potential-energy surfaces that have been used successfully to calculate fission-fragment mass distributions [10,11,16,20]. This novel treatment has considerable predictive power and can readily be applied to other fission cases as well, including cases where no experimental data yet exist.

## Acknowledgement

This work was supported by the Swedish Natural Science Research Council (S.Å.) and the Knut and Alice Wallenberg Foundation (M.A., B.G.C. and S.Å.); J.R. was supported in part by the NNSA

DNN R&D of the U.S. Department of Energy and acknowledges Visiting Professorships at the Division of Mathematical Physics at Lund University and at the Yukawa Institute for Theoretical Physics at the University of Kyoto.

## References

- [1] O. Hahn, F. Straßmann, *Naturwissenschaften* 27 (1939) 11.
- [2] L. Meitner, O.R. Frisch, *Nature (London)* 143 (1939) 239.
- [3] A.N. Andreyev, K. Nishio, K.H. Schmidt, *Rep. Prog. Phys.* 81 (2018) 016301.
- [4] K.H. Schmidt, B. Jurado, *Rep. Prog. Phys.* 81 (2018) 106301.
- [5] N. Schunck, L.M. Robledo, *Rep. Prog. Phys.* 79 (2016) 116301.
- [6] P. Talou, R. Vogt, J. Randrup, M.E. Rising, S.A. Pozzi, J. Verbeke, M.T. Andrews, S.D. Clarke, P. Jaffke, M. Jandel, T. Kawano, M.J. Marcat, K. Meierbachtol, L. Nakae, G. Rusev, A. Sood, I. Stetcu, C. Walker, *Eur. Phys. J. A* 4 (2018) 9.
- [7] N. Bohr, J.A. Wheeler, *Phys. Rev.* 56 (1939) 426.
- [8] H.A. Kramers, *Physica* 7 (1940) 284.
- [9] J. Blocki, Y. Boneh, J.R. Nix, J. Randrup, M. Robel, A.J. Sierk, W.J. Swiatecki, *Ann. Phys.* 113 (1978) 330.
- [10] J. Randrup, P. Möller, *Phys. Rev. Lett.* 106 (2011) 132503.
- [11] J. Randrup, P. Möller, A.J. Sierk, *Phys. Rev. C* 84 (2011) 034613.
- [12] A. Bulgac, P. Magierski, K.J. Roche, I. Stetcu, *Phys. Rev. Lett.* 116 (2016) 122504; A. Bulgac, S. Jin, I. Stetcu, *Phys. Rev. C* 100 (2019) 014615.
- [13] A. Bulgac, S. Jin, K.J. Roche, N. Schunck, I. Stetcu, *Phys. Rev. C* 100 (2019) 034615.
- [14] Y. Tanimura, D. Lacroix, G. Scamps, *Phys. Rev. C* (2015) 034601.
- [15] J. Randrup, P. Möller, A.J. Sierk, *Phys. Rev. C* 85 (2012) 024306.
- [16] J. Randrup, P. Möller, *Phys. Rev. C* 88 (2013) 064606.
- [17] P. Möller, J. Randrup, A. Iwamoto, T. Ichikawa, *Phys. Rev. C* 90 (2014) 014601.
- [18] P. Möller, T. Ichikawa, *Eur. Phys. J. A* 51 (2015) 173.
- [19] P. Möller, A.J. Sierk, T. Ichikawa, A. Iwamoto, R. Bengtsson, H. Uhrenholt, S. Åberg, *Phys. Rev. C* 79 (2009) 064304.
- [20] D.E. Ward, B.G. Carlsson, T. Døssing, P. Möller, J. Randrup, S. Åberg, *Phys. Rev. C* 95 (2017) 024618.
- [21] K.H. Schmidt, B. Jurado, *Phys. Rev. Lett.* 104 (2010) 212501.
- [22] D.G. Madland, J.R. Nix, *Nucl. Sci. Eng.* 81 (1982) 213.
- [23] S. Lemaire, P. Talou, T. Kawano, M.B. Chadwick, D.G. Madland, *Phys. Rev. C* 72 (2005) 024601.
- [24] N.V. Kornilov, F.-J. Hamsch, A.S. Vorobeyev, *Nucl. Phys. A* 789 (2007) 55.
- [25] H.A. Bethe, *Phys. Rev.* 50 (1936) 332.
- [26] J.R. Nix, *Nucl. Phys. A* 130 (1969) 241.
- [27] M. Albertsson, B.G. Carlsson, T. Døssing, P. Möller, J. Randrup, S. Åberg, in preparation.
- [28] P. Möller, A.J. Sierk, A. Iwamoto, *Phys. Rev. Lett.* 92 (2004) 072501.
- [29] H. Uhrenholt, S. Åberg, A. Dobrowolski, T. Døssing, T. Ichikawa, P. Möller, *Nucl. Phys. A* 913 (2013) 127.
- [30] K. Nishio, Y. Nakagome, H. Yamamoto, I. Kimura, *Nucl. Phys. A* 632 (1998) 540.
- [31] V.F. Apalin, Y.N. Griityuk, I.E. Kutikov, V.I. Lebedev, L.A. Mikaelian, *Nucl. Phys. A* 71 (1965) 553.
- [32] A.S. Vorobeyev, et al., *EPJ Web Conf.* 8 (2010) 3004.
- [33] O.I. Batenkov, et al., *AIP Conf. Proc.* 769 (2005) 625.
- [34] J.W. Boldeman, A.R. de L. Musgrove, R.L. Walsh, *Aust. J. Phys.* 24 (1971) 821.
- [35] E.E. Maslin, A.L. Rodgers, W.G.F. Core, *Phys. Rev.* 164 (1967) 1520.
- [36] A. Göök, F.J. Hamsch, S. Oberstedt, *EPJ Web Conf.* 169 (2018) 4.
- [37] G. Scamps, C. Simenel, *Nature* 564 (2018) 382.
- [38] B.D. Wilkins, E.P. Steinberg, R.R. Chasman, *Phys. Rev. C* 14 (1976) 1832.
- [39] N. Dubray, H. Goutte, J.-P. Delaroche, *Phys. Rev. C* 77 (2008) 014310.
- [40] J. Randrup, R. Vogt, *Phys. Rev. C* 80 (2009) 024601.
- [41] R. Müller, A.A. Naqvi, F. Käppeler, F. Dickmann, *Phys. Rev. C* 29 (1984) 885.